High-Speed Wide-Field Imaging of Microcircuitry Using Nitrogen Vacancies in Diamond

Webb, James L.; Troise, Luca; Hansen, Nikolaj W.; Frellsen, Louise F.; Osterkamp, Christian; Jelezko, Fedor; Jankuhn, Steffen; Meijer, Jan; Berg-Sørensen, Kirstine; Perrier, Jean François

Total number of authors:
12

Published in:
Physical Review Applied

Link to article, DOI:
10.1103/PhysRevApplied.17.064051

Publication date:
2022

Document Version
Publisher's PDF, also known as Version of record

High-Speed Wide-Field Imaging of Microcircuitry Using Nitrogen Vacancies in Diamond

James L. Webb,[1,*] Luca Troise,[1] Nikolaj W. Hansen,[2] Louise F. Frellsen,[1] Christian Osterkamp,[3] Fedor Jelezko,[3] Steffen Jankuhn,[4] Jan Meijer,[4] Kirstine Berg-Sørensen,[5] Jean-François Perrier,[2] Alexander Huck,[1,†] and Ulrik Lund Andersen[1,‡]

[1] *Center for Macroscopic Quantum States (bigQ), Department of Physics, Technical University of Denmark, Kongens Lyngby 2800, Denmark*

[2] *Department of Neuroscience, Copenhagen University, Copenhagen 2200, Denmark*

[3] *Institute for Quantum Optics and Center for Integrated Quantum Science and Technology (IQST), Ulm University, Albert-Einstein-Allee 11, Ulm 89081, Germany*

[4] *Division of Applied Quantum Systems, Felix Bloch Institute for Solid State Physics, Leipzig University, Leipzig 04103, Germany*

[5] *Department of Health Technology, Technical University of Denmark, Kongens Lyngby 2800, Denmark*

(Received 28 August 2021; revised 4 February 2022; accepted 5 May 2022; published 27 June 2022)

The ability to measure the passage of electrical current with high spatial and temporal resolution is vital for applications ranging from inspection of microscopic electronic circuits to biosensing. The ability to image such signals passively and remotely is of great importance, in order to measure without invasive disruption of the system under study or the signal itself. A recent approach to achieving this utilizes point defects in solid-state materials; in particular, nitrogen-vacancy centers in diamond. Acting as a high-density array of independent sensors, addressable opto-electronically and highly sensitive to factors including temperature and magnetic field, these are ideally suited to microscopic wide-field imaging. In this work, we demonstrate simultaneous spatially and temporally resolved recovery signals from a microscopic lithographically patterned circuit. Through application of a lock-in amplifier camera, we demonstrate micrometer-scale imaging resolution with a millimeter-scale field of view with simultaneous spatially resolved submillisecond (up to 3500 frames s^{-1}) recovery of dc to kilohertz alternating and broadband pulsed-current electrical signals, without aliasing or undersampling. We demonstrate as examples of our method the recovery of synthetic signals replicating digital pulses in integrated circuits and signals that would be observed in a biological neuronal network in the brain.

DOI: 10.1103/PhysRevApplied.17.064051

I. INTRODUCTION

Microscopic electrical transport underpins both synthetic systems such as integrated circuits as well as biological processes including the functioning of the human brain and nervous system. Operating at high speed and relying on transport down to single electronic charges, these systems require advanced inspection tools, in order to monitor transport performance and diagnose faults. In the case of a synthetic circuit, faults arising from factors including poor insulation and electromigration [1] can reduce the device lifetime, requiring intervention before failure. Equivalently, in a biological system, faults at the microscopic level arising from disease (e.g., Alzheimer's) can have serious consequences if left undetected.

Key to microscopic inspection are techniques capable of simultaneously spatially and temporally resolving electrical transport, ideally noninvasively, without causing damage to the current path or surrounding material. Existing methods for integrated circuit inspection such as laser voltage probing [2], electron microscopy [3], terahertz spectroscopy [4] and electrophysiology probes [5], or fluorescence microscopy [6] for biosystems require unimpeded local access and direct active interaction with the target system. This active sensing has the potential to interfere with the target signal or, at worst, induce damage in the system under study.

What is desirable is an inspection tool that is passive, remote, and noninvasive. In recent years, a technique has emerged for this purpose, utilizing point defects in solid-state materials. Located in a solid material at a distance

*jaluwe@fysik.dtu.dk
†alexander.huck.dtu.dk
‡ulrik.andersen@fysik.dtu.dk

from the signal source under study, these can act as atomic scale (quantum) sensors to remotely and passively probe factors including the electric field [7], the temperature [8], the pressure and/or strain [9], motion [10,11], and, in particular, the magnetic field [12–14]. State-of-the-art measurements are based on negatively charged nitrogen-vacancy (N-V) centers in diamond [15]. Consisting of a substitutional nitrogen dopant paired with a lattice vacancy, these defects have an energy-level structure that is highly sensitive to environmental factors. Sensing using N-V centers can be performed by monitoring the fluorescence output of a single N-V or an ensemble of N-Vs in a diamond under a green laser and microwave irradiation via optically detected magnetic resonance (ODMR) spectroscopy [16,17]. Acting as a high-density array of independent sensors, N-V centers are ideally suited for wide-field imaging using fluorescence emission, particularly imaging of the magnetic field arising from electrical circuits [18,19], electronic transport in graphene [20,21], ferromagnetic geological samples [22], and in biological systems [23–25] and the passage of signals in a living biological neural network [26,27].

However, state-of-the-art imaging with N-V centers suffers from two disadvantages. The first is that the level of state-of-the-art per-pixel sensitivity realized experimentally is as yet insufficient to resolve the picotesla- to nanotesla-level signals necessary for these applications, although theoretical camera limits indicate that measurement of fields in this range should be possible [28]. This is compounded by restrictions in the field of view as well as artifacts and background noise [29]. The second disadvantage is that limitations in measurement methods prohibit the simultaneous spatial and temporal resolution of the desired signals, required to recover key properties capable of giving new systematic insights, including the temporal shape, relative size, and latency of the signal. In particular, limitations such as low camera frame rates constrain the temporal bandwidth of recording, prohibiting the recovery of broadband (pulsed) signals typical of applications, with frequency components spanning the dc to kilohertz range. Imaging has therefore been limited to slow (20–200 Hz) or static field measurements, including the temperature [19,30] or the dc magnetic field from ferromagnetic materials [31–33], or has relied on signal aliasing [34], which is unsuitable for accurate time-resolved signal recovery.

In this work, we solely address the second of these limitations. Through application of a lock-in amplifier camera (Helicam, Heliotis AG [28,35,36]), we image N-V centers in diamond to simultaneously spatially and temporally resolve the absolute magnitude of the magnetic field induced by electric current in a lithographically patterned microcircuit. We demonstrate the viability of our technique to image current in the circuit with a wider field of view (millimeter scale) than previously realized, with micrometer-level resolution, while recording spatially resolved signals with high (submillisecond) temporal resolution. We show that this can be done with a simple constant laser and microwave (continuous-wave, cw) method and that we can overcome inhomogeneity; in particular, nonuniform laser illumination at the Brewster angle for diamond. We demonstrate imaging of single-frequency ac signals up to 1.5 kHz and recover these signals with simultaneous submillisecond resolution in the time domain. These signals are significantly faster than those imaged and recovered in equivalent state-of-the-art experiments in the field. We demonstrate signal recovery above the single-pixel noise floor in image regions of the diamond both directly adjacent to and well away from the patterned wire. Finally, we exemplify our technique by recording broadband signals that replicate digital pulsed signals in integrated circuits and current signals of the shape of field-excitatory postsynaptic potentials (fEPSPs) in the hippocampus of the living brain.

II. METHODS

A simplified schematic of our setup is shown in Fig. 1. We use a 2×2 mm^2 electronic grade diamond (Element 6) with a top 1 μm {100}-oriented chemical-vapor-deposition (CVD) overgrown layer with approximately 99.99% ^{12}C and 10 ppm (parts per million) ^{15}N doping. The diamond is irradiated with He^+ at 1.8 MeV, using a dose of 10^{15} cm^{-2}, followed by annealing at 900 °C. We measure the N-V concentration to be in the range 0.1–1 ppm. The fluorescence emission of this diamond, measured using a photodiode power meter (Thorlabs S120C) in place of the camera, is measured to be $P_{\mathrm{fl}} = 152$ μW under 1.8 W of green-pump-laser power, a relatively low level as compared to state-of-the-art schemes [37].

We fabricate the circuit on either Si or glass substrate, patterned using ultraviolet-mask-aligned photolithography and metalized by deposition of Ti-Au. The track widths are 30 μm, decreasing to 6 μm in a 30×30 μm^2 square region at the center of the cross. We mount the diamond and circuit on a printed-circuit-board (PCB) microwave antenna with a hole through which laser light can be directed into the diamond, which is mounted directly onto the PCB using Kapton tape. We mount the diamond with the N-V center layer at the surface adjacent to where we attach the circuit, using a small amount of acrylate glue or a 3D-printed plastic holder. The separation between the diamond and the circuit is measured to be 10 μm, by adjusting the imaging focal plane between the circuit and the bottom facet of the diamond using a micrometer optomechanical stage.

Up to 1.8 W of green pump light can be supplied to the diamond at the Brewster angle using a diode pumped solid-state laser (Cobolt Samba). Light is directed to the diamond via a focusing lens (Thorlabs LB1676), defocused slightly in order to achieve more uniform

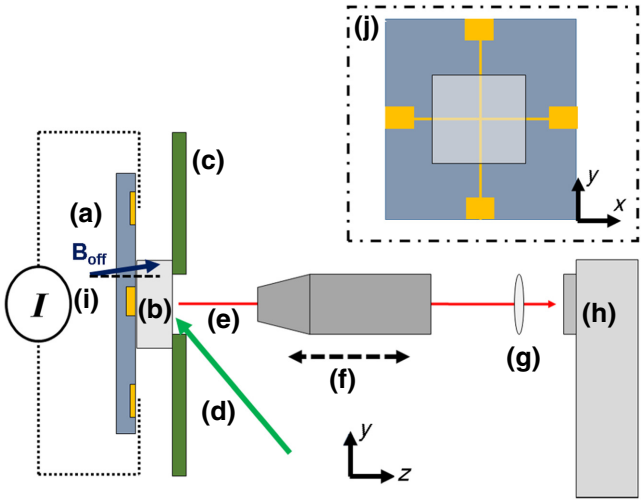

FIG. 1. A simplified side-on and camera-perspective schematic of the experimental setup (not to scale). The lithographically patterned circuit cross on a Si or glass substrate (a) is placed adjacent to the diamond (b) and affixed using either acrylate glue or a three-dimensionally (3D) printed plastic holder. The diamond and circuit are then affixed to a printed-circuit-board (PCB) microwave antenna (c) with a hole to allow pump laser (d) to reach the diamond at the Brewster angle and fluorescence collection (e) via a translatable microscope objective (f). The fluorescence is focused (g) into the lock-in camera (h) to produce an image of the circuit. Current (i) is applied through the circuit using contacts soldered to the circuit chip. The view from the perspective of the camera is detailed in (j), with the diamond on the center of the cross tracks. We apply a static offset field $\mathbf{B}_{off}$ from behind the diamond front face (x,y), oriented off the z axis but with a majority component in z, in order to split the resonances of the four different N-V axes.

illumination across the diamond. Fluorescence collection is achieved using a long-working-distance microscope objective (Motic, 10X/0.28, working distance 33.5 mm) placed in front of the diamond N-V layer and mounted on a micrometer translation stage ($\pm$10 mm travel) to achieve focus control, with a second coarse-adjustment stage to control lateral optical alignment and a screw post for vertical alignment. Light collected by the objective is passed through a long-wavelength pass filter (Thorlabs FELH0600) mounted in a beam tube to remove the 532-nm pump-laser light, leaving only the emitted N-V center fluorescence. A second lens (Thorlabs LA1484) with a 300-mm focal length placed in the beam tube 30 mm behind the objective focuses this light into the aperture of the camera (infinite conjugate configuration), with the camera placed at the end of the beam tube 145 mm behind the tube lens. For fluorescence detection, we use a lock-in amplifier camera (Heliotis Helicam C3 [35]), running at a rate of up to 3500 frames s^{-1}. Although heat sunk to the optical table and capable of 3800 frames s^{-1}, we run the camera at this reduced frame rate due to concerns regarding overheating during long-period acquisitions.

In the Supplemental Material [38], we include a complete step-by-step breakdown of our circuit-measurement procedure. As a first step, we use the intensity mode of the camera to align and focus onto the circuit and diamond. In intensity mode, the camera operates like any conventional digital camera, with the recorded signal from each pixel depending on the intensity of light that pixel receives. We find that the fluorescence emission of the diamond is sufficiently bright to clearly see the circuit, without additional external illumination. Our field of view projected onto the (300 $\times$ 300)-pixel sensor area (292 $\times$ 280 usable, surrounded by edge test pixels) with a 10$\times$ objective is approximately 1.5 $\times$ 1.5 mm^2, with each pixel covering an area of the circuit and diamond of approximately 5 $\times$ 5 μm^2. The magnification can be increased if required by the simple replacement of the microscope objective and eyepiece lens.

For subsequent measurements, we use the camera in lock-in mode. In this mode, the camera produces a square-wave reference signal f_{mod} at a user-defined frequency (up to 14 KHz in this work). This is connected to a microwave generator (Stanford SG380), supplying amplified (Minicircuits ZHL-16W-43+) microwaves of frequency f_{MW} to the diamond via a PCB antenna. We use the reference signal to frequency modulate the microwaves supplied to the diamond, with a modulation deviation of amplitude f_{dev} from f_{MW}. When at a microwave frequency corresponding to a N-V center resonance, the microwave modulation produces modulation at f_{mod} of the fluorescence light emitted by the N-V centers, by driving the N-V centers on and off the dip in fluorescence output associated with the ODMR resonance.

In lock-in camera mode, each individual pixel captures this variation in fluorescence intensity and the camera demodulates it against the reference signal f_{mod}. This gives a 10-bit digitized value p_v proportional to the amplitude of the modulated fluorescence signal, defined by the contrast of the ODMR resonance at a given f_{MW}. Fundamentally, this principle of the camera operation is identical to the method of bulk sensing using a single photodiode and integrating all fluorescence emission from the diamond [12,37]. Each pixel effectively acts as if it was a single independent photodiode, lock-in amplifier, and digitizer. However, each pixel is only illuminated by N-V fluorescence from one part of the diamond, allowing spatially and temporally resolved imaging of changes in fluorescence emission, produced by the magnetic field from the circuit at the diamond. The lock-in camera allows significant rejection of noise from sources away from f_{mod}, particularly pump-laser dc and low-frequency technical noise.

Using the lock-in mode, we measure the ODMR spectrum by averaging p_v over all image pixels while sweeping microwave frequency $f_{MW} = 2700 - 3100$ MHz in 0.5-MHz steps. This is performed first without an offset field and then with a several-millitesla static magnetic

field B_{off} to split the N-V resonances in microwave frequency for each of the four N-V–center crystallographic directions (eight resonance frequencies in total) [22,39,40]. This field is applied using a 1.5-in.-square neodymium permanent magnet behind the diamond circuit assembly and is approximately 4 mT (122-MHz ODMR resonance-frequency shift) in magnitude in the projection of the N-V axis used for measurement. Through repeated ODMR scans while adjusting the magnet, we align the magnet with the diamond and optimize the offset magnet position to also minimize the field gradient, measured as a shift in resonance frequency across the imaged region of the diamond.

We then optimize the modulation frequency deviation f_{dev} to give the maximum contrast and slope dp_v/df_{MW} in the all-pixel average ODMR spectrum. Maximization of the slope ensures the greatest possible change in fluorescence and signal p_v as a result of any additional magnetic field from the wire circuit, maximizing the experimental sensitivity. We find the optimum $f_{\text{dev}} = 2$ MHz peak-to-peak (± 1 MHz amplitude, centered on f_{MW}), a value ultimately defined by the line width of the ODMR resonance.

We then select a single N-V resonance in our ODMR spectrum, defining a single axis for our measurements. The possible axes and measurement direction in this work are detailed in Fig. 3 of the Supplemental Material [38]. We use the resonance with the maximum frequency shift produced by the static offset field with respect to the zero-field resonance frequency (2.88 GHz), in the direction of the microwave antenna central resonance frequency (2.6–2.7 GHz) in order to maximize the microwave power transmission to the N-V centers. To precisely identify the frequency $f_{\text{MW}} = f_{\text{max}}$ corresponding to the maximum ODMR slope dp_v/df_{MW}, we then perform a high-resolution ODMR scan centered on this resonance $\pm 0.5 - 2$ MHz in 0.1 MHz steps. All subsequent circuit magnetic field imaging is then performed at this microwave frequency f_{max}, delivering the maximum overall sensitivity. By recording p_v as a function of f_{MW} for all pixels separately in our high-resolution scan, this procedure allows us to recover in detail the full ODMR spectrum for each pixel and allows recovery of the magnetic field in tesla units for each pixel, using the conversion factor $df/dB = 28\ \text{Hz}\,\text{nT}^{-1}$ [41].

Note that the pixel values acquired from the camera in lock-in mode are offset by an intrinsic hardware value specific to each pixel. We measure and subtract this offset by taking a reference image well off microwave resonance (at $f_{\text{MW}} = 2600$ MHz) and with the circuit grounded through a switch box, ensuring no signal. This is performed after obtaining the ODMR spectrum. All values of p_v reported in this work have this hardware offset subtracted.

Imaging of the circuit is performed at different microwave modulation frequencies ($f_{\text{mod}} = 2.5$ kHz to 14 kHz) and camera frame rates (650–3500 frames s^{-1}). For each measurement, we take 500 continuous frames (the maximum memory capacity of the camera), giving a time series for each camera pixel. The data are then transferred to a personal computer (PC) via USB 2.0, taking up to 8 s per 500-frame acquisition. Each time series can then be processed individually, to show the presence of the desired pulsed signal in the time domain, or fast Fourier transformed to recover the frequency and magnitude of the ac signal. When necessary, we can apply noise-filtering techniques derived from our bulk–N-V–sensing experiments [29,42] to these time series, allowing the reduction of background magnetic noise, in particular the primary and 3rd harmonic of electrical mains at 50 Hz and 150 Hz (60 Hz/180 Hz in North America) without the need to magnetically shield the setup. Either the ac or the pulse magnitude recorded by each pixel can then be used to generate an image of the total magnetic field seen by the N-V centers across the field of view.

Signals are generated in the cross circuit using a current source (Keithley 6221), supplying leads soldered to four pads patterned on the circuit substrate. The current source is used to generate ac square-wave signals as well as pulsed and synthetic biosignals using an in-built arbitrary waveform generation (AWG) capability. Currents ranging from 1 mA up to 100 mA are applied to the circuit. No visible drift in resonance frequency associated with the temperature increase due to resistive heating is observed in the ODMR traces. We use a voltage trigger (NI-DAQ 6221) that sets a constant (zero) phase for the applied ac signals at the start of each 500-frame acquisition, ensuring a fixed phase for repeated acquisitions for signal averaging. Although not implemented in this work, we could also recover signals of arbitrary phase by obtaining separate in-phase and quadrature value (I and Q) components from the camera, with $p_v = \sqrt{I^2 + Q^2}$.

To provide the hippocampus biosignal to be replicated in our circuit, brain slices are obtained from adult (4–8 weeks) C57BL/6 mice (Janvier, France). Briefly, following isoflurane anesthesia, mice are decapitated and their brains dissected, submerged in ice-cold carbogen- (95% O_2-5% CO_2) saturated sucrose-substituted artificial cerebrospinal fluid (sACSF), containing sucrose (200 mM), $NaHCO_3$ (25 mM), glucose (11 mM), KCl (3 mM), $CaCl_2$ (0.1 mM), $MgCl_2$ (4 mM), KH_2PO_4 (1.1 mM), sodium pyruvate (2 mM), myoinositol (3 mM), and ascorbic acid (0.5 mM). 300-μm-thick sagittal brain slices are cut in ice-cold sACSF using a VT1200s Vibratome (Leica, Germany). The slices are allowed to recover for at least 90 min in an interface-type holding chamber, continuously bubbled with carbogen, kept at 28 °C and filled with regular ACSF, containing NaCl (111 mM), $NaHCO_3$ (25 mM), glucose (11 mM), KCl (3 mM), $CaCl_2$ (2.5 mM), $MgCl_2$ (1.3 mM), and KH_2PO_4 (1.1 mM).

Individual slices containing the hippocampus are transferred to a custom-made submerged-type recording

chamber continuously perfused with carbogen-saturated ACSF. The fEPSPs are evoked by stimulating the Schaffer collaterals at 0.05 Hz using 0.05-ms current pulses delivered through a twisted Pt-Ir wire electrode, connected to an A365 stimulus isolator (WPI, USA) and placed in the stratum radiatum at the border between the CA3 and CA1 regions. The fEPSPs are recorded using an ACSF-filled glass electrode (4–6 MΩ), connected to a CV-7B headstage (Molecular Devices, USA) and placed in the stratum radiatum region of CA1. The fEPSP signals are amplified using a 700B amplifier (Molecular Devices, USA) and digitized for recording (NI-DAQ 6221). Examples of these measurements are detailed in the Supplemental Material [38].

III. RESULTS

A. Intensity and ODMR

We first align and focus the camera and collection optics to give a clear centered image of the circuit. This is achieved by a simple recording of the N-V fluorescence intensity at 50 frames s^{-1} while adjusting the alignment. Figure 2(a) shows the circuit imaged using the intensity of the N-V fluorescence emitted by the diamond without using the lock-in capability (camera intensity mode), with the conductive Ti-Au tracks of the circuit brighter due to the fact that they reflect more of the fluorescence generated in the adjacent N-V layer. By performing ODMR spectroscopy in intensity mode, we estimate the all-pixel average contrast on microwave resonance to be 1.2–1.6%. As detailed in Sec. II, we then use the lock-in capability of the camera, with frequency modulation of the microwaves supplied to the diamond, to perform ODMR spectroscopy. Selecting a single microwave resonance with the strongest response (the greatest frequency shift) to the majority out-of-plane static offset magnetic field, we then perform a detailed step scan (0.05-MHz step, 500 frames per point) across the frequencies with the maximum ODMR spectral slope dp_v/df_{MW} for each pixel. The response, obtained by averaging the ODMR spectrum from all pixels can be seen in Fig. 2(b). For each pixel, a slightly different ODMR spectrum is recorded due to local broadening effects including strain or variations in the offset field, resulting in the less-than-smooth slope in the figure. Examples of measured single-pixel ODMR spectra can be seen in the Supplemental Material [38]. The degree of resonance-frequency variation is < 0.2 MHz across the image. This allows us to extract dp_v/df_{MW} for each pixel using an ODMR scan of 1–2 MHz across the resonance and to remain sensitive (close to the maximum slope) for the majority of pixels using only a single fixed microwave frequency ($f_{\mathrm{max}} = 2758.7$ MHz).

We select a single resonance in this manner due to the significant amount of time required to capture the full ODMR spectrum covering all N-V microwave resonances via the relatively slow data-transfer rate of the camera. If faster transfer speeds were available, it would be possible to perform spatially resolved vector sensing in the manner similar to that outlined in the work by Schloss *et al.* [43], by recording from each microwave resonance in turn. However, the use of a single N-V axis gives a simple and useful measure of the magnitude of the magnetic field at that point in the image and hence the magnitude of the current flow in the adjacent circuit. Note that the ODMR

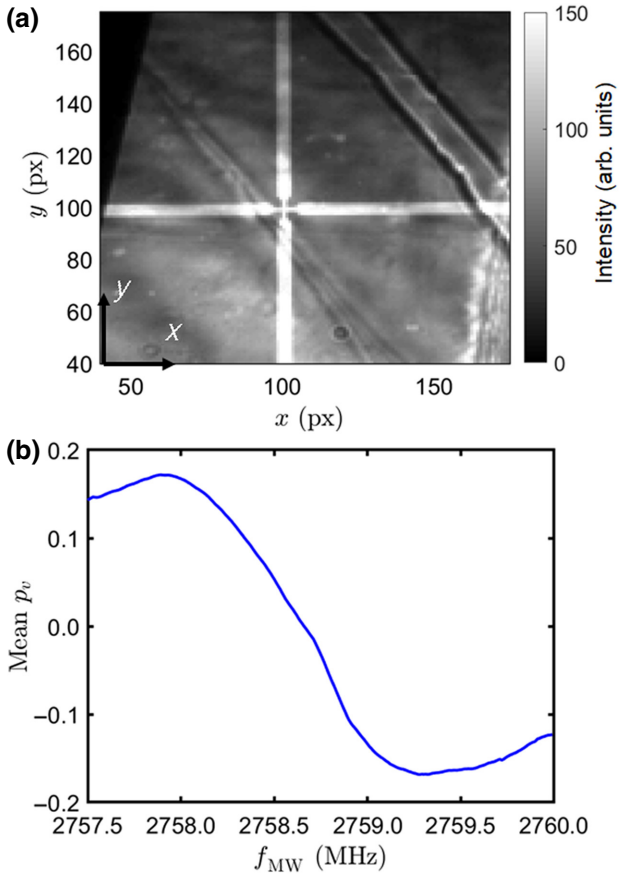

FIG. 2. (a) The brightness of fluorescence from the diamond measured in camera intensity mode in an enlarged region around the cross-circuit center. Throughout this work, 1 pixel (px) $\approx 5 \times 5$ μm on the circuit, derived by comparing the image to the patterned-circuit-feature dimensions. The edge of the diamond can be seen as the black area in the upper left of the image. The feature across the upper right is a surface-contamination artifact (residual glue on the circuit substrate). (b) ODMR spectroscopy in camera lock-in mode, plotted as the mean of pixel values p_v averaged across the whole image versus the microwave drive frequency f_{MW}. We measure while centered on a single microwave resonance (single N-V axis). This reference ODMR could be used to convert into real (tesla) units of magnetic field for each pixel. Note that in (b), we average over all pixels in the image, even those with signal-to-noise ratio (SNR) < 1, which leads to a mean value of p_v less than the minimum digitization level ($= 14$).

spectrum is only required for magnetic field unit conversion. For the majority of relevant applications, often only the relative signal (shape, current path, on-off) is necessary. This can be achieved more simply by taking a fast ODMR trace to find the point of maximum sensitivity $f_{\max}$ at the maximum ODMR slope and recording the relative response in terms of the unitless change in p_v.

B. Alternating-current imaging

In Figs. 3(a) and 3(b), we show example images of the magnetic field, arising from a constant 130-Hz alternating current passed through the cross circuit in either the vertical (y) or the horizontal (x) direction. This current replicates the lower-frequency current typical of transmission in power lines (i.e., 50/60 Hz) and odd inductive harmonics (e.g., 150/180 Hz). We use a microwave modulation rate of $f_{\text{mod}} = 2.5$ kHz, close to the slowest possible camera modulation rate, and a frame rate of 650 frames s^{-1}, delivering the best average per-pixel signal-to-noise ratio (SNR) for the target signal. As expected, we observe the strongest response from the N-V centers directly adjacent to the circuit, dropping rapidly away from the wire position. This response is only observed in the directions through the cross where current flows, this direction being indicated in the figures by green arrows. We clearly observe the change in the magnetic field resulting from track-width reduction in the cross center, in both current directions. As we image a projection of the field along a single (out-of-circuit-plane) N-V axis, the field response is much greater in the vertical (y) current direction, which allows higher SNR recovery at lower current than with current in the horizontal (x) direction.

In order to validate our images, we calculate the relative strength of the field covering the entire camera field of view (approximately 1.5×1.5 mm^2). Modeling as an

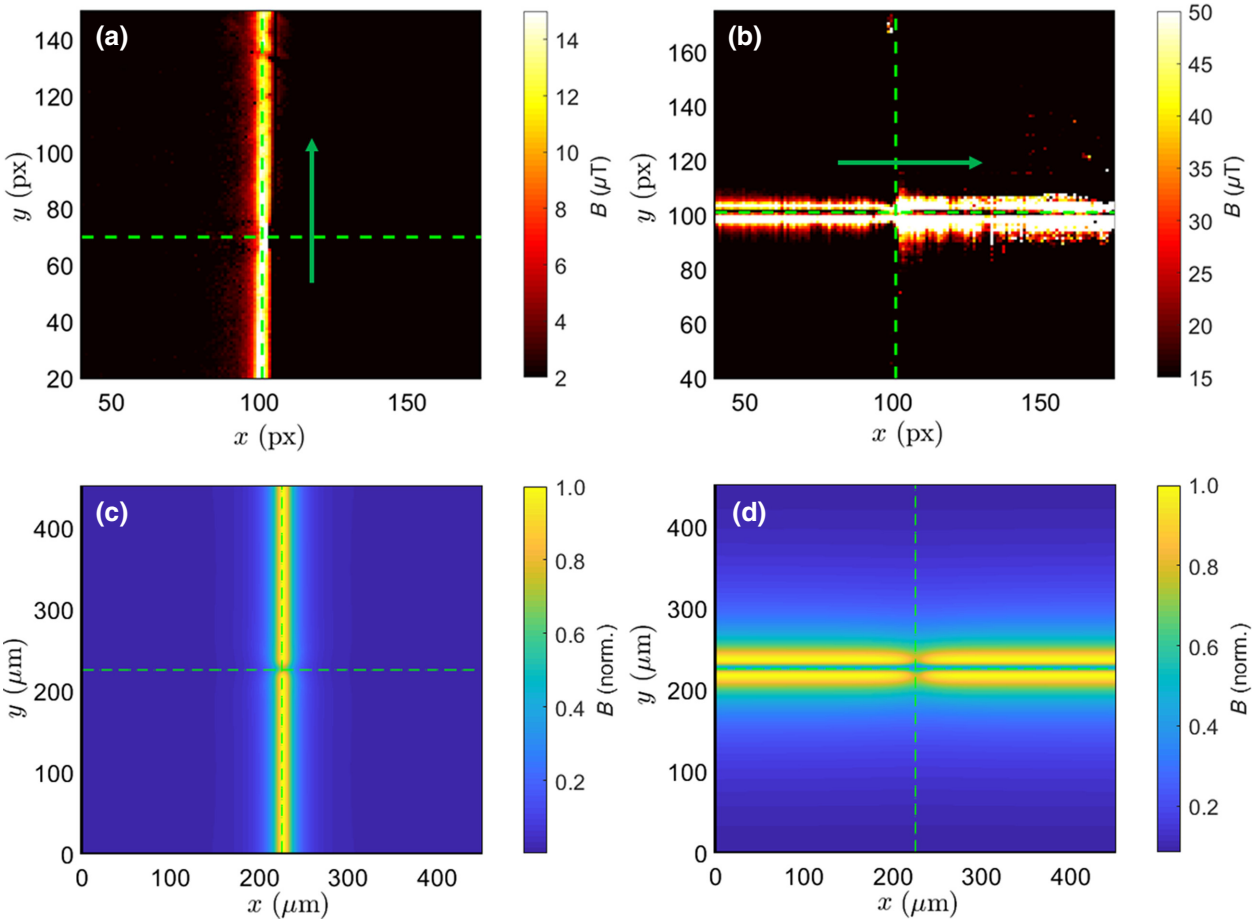

FIG. 3. (a) The imaged magnetic field resulting from a 130-Hz 4-mA alternating current in the vertical (y-axis) cross direction and (b) from a 130-Hz 20-mA current in the horizontal (x-axis) direction. The direction of current flow through the cross is indicated by the green arrow on the figure. We plot the response only from pixels (px) with SNR > 3, in order to clearly distinguish the signal from background noise in the images. (c),(d) A strong response is imaged from the N-V centers directly adjacent to the current-carrying wire tracks, which can be qualitatively replicated by first-principles modeling of the expected field strength. The location of the cross is shown as a dashed line. The higher noise to the right-hand side of the cross in (b) as compared to the left-hand side is an artifact due to higher noise from a block of camera pixels in this region.

infinitely long wire of elements dl carrying current I (full details are given in the Supplemental Material [38]), we calculate the field strength projected along an N-V axis best aligned with the predominantly out-of-plane (z direction) dc offset field. Figures 3(c) and 3(d) show these plots of the calculated relative magnetic field, normalized to the maximum in the modeled field of view, assuming a circuit–N-V separation of 10 μm. The modeled images strongly replicate the experimental images, particularly the central narrowing and the strip of relatively low magnetic field near the wire track with current in the horizontal (x) direction, where the magnetic field vector at the N-V layer points away from the sensitive N-V axis.

To further test the magnetic field recording, we image the cross at a applied current values in the range $I = 1 - 20$ mA. In Fig. 4, the amplitude spectrum of the signal can be seen, extracted from a 500-frame time series for each pixel and then averaged across the image. Examples of the spectra for individual pixels across the image are given in the Supplemental Material [38]. The primary (130-Hz) and second (260-Hz) harmonic of the current signal are both observed and the change in signal amplitude at 130 Hz as a function of the current can be seen in Fig. 5. By increasing the camera modulation rate and frame rate, we are able to acquire ac signals of frequency up to 490 Hz (at $f_{\mathrm{mod}} = 6$ kHz microwave modulation, 1000 frames s^{-1}) and up to 1.51 kHz (at $f_{\mathrm{mod}} = 14$ kHz microwave modulation, 3500 frames s^{-1}). Examples of these can be seen in the Supplemental Material [38].

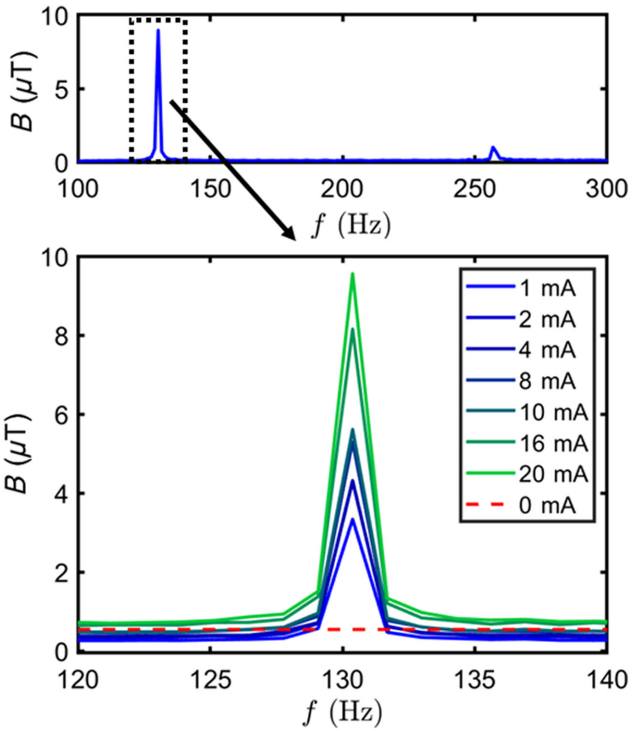

FIG. 4. The spectrum of the current signal extracted from the FFT of a 500-frame-length time series, averaging spectra taken from all usable pixels (292 × 280). Both the 130-Hz primary and the 260-Hz second harmonic are visible. The signal is observed to reduce in strength with lower current, as expected for the magnetic field from a current-carrying wire. We plot the noise floor in the spectrum from a measurement at $I = 0$ mA. This primarily arises from readout and $1/f$ laser technical noise. At 130 Hz, this floor appears as an artifact offset field of approximately 0.55μT, when in reality there is no signal. We subtract this artifact from the data points presented in Fig. 5.

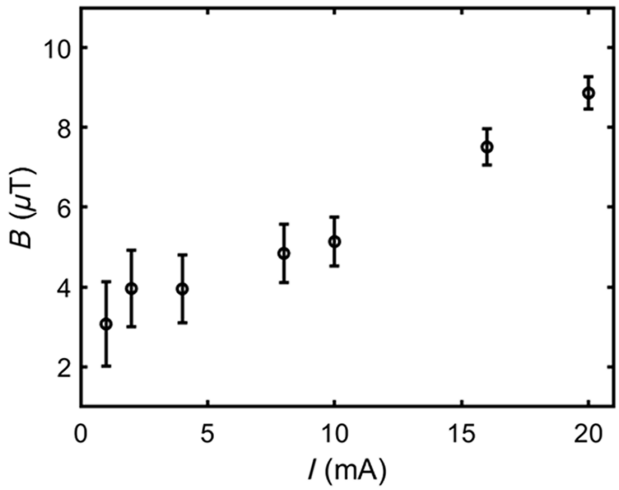

FIG. 5. The maximum strength of the 130-Hz signal from the averaged spectra in Fig. 4 as a function of the current. We consider that in the higher-current regime (> 2.5 mA in our setup), the signal scales linearly with the applied current, as should be expected from the magnetic field induced by a single current-carrying wire. In the low-current region, the weaker signal drops below the noise floor for increasing numbers of pixels, nonlinearly reducing the camera signal and leading to an underestimate of the magnetic field B in this regime.

We expect the ac signal magnitude to scale linearly with current, as would be expected from a simple model of a single current-carrying wire. However, the fitting of a linear trend to our data in Fig. 5 implies an unphysical nonzero signal at $I = 0$. We consider that this can be explained by assuming two sensing regimes. In the first, at higher current, we have a strong signal in the majority of pixels imaging from the wire region, such that the camera correctly records the magnitude of B and the linear scaling of the magnetic field with the applied current I. In the second regime, at low current, technical limitations in the readout method impact the measurement as the (weaker) signal drops below the noise floor in an increasing number of pixels. In this regime, this leads to increased readout noise, nonlinear scaling of B versus I, and an underestimate of the magnetic field magnitude. In the Supplemental Material [38], we present a simple model of this behavior, estimating the point at which the technical limits of the camera readout begin to impact the measurement to

be at approximately 2.5 mA for our setup. We ensure that later tests of pulsed sensing are well above this threshold, to ensure accurate recovery of the magnetic field amplitude. Note that this limit is purely technical and is specific to our setup, rather than being a physical barrier, and will be lowered by factors such as enhanced diamond ODMR contrast. Furthermore, it is only a problem for a measurement averaged over many pixels, as a single individual pixel will accurate record the field strength until the signal drops below the noise floor specific to that pixel. We also note that this is only a problem if the absolute magnitude of the field at very low current is required. In many cases (e.g., digital logic or in biological neural networks), it is only necessary to capture the shape or the presence or absence of a signal pulse in the time domain.

C. Pulsed current

In order to demonstrate the detection of a digital signal as typical for an integrated circuit, we apply a series of 20-mA current pulses of forward (reverse) polarity and 1-ms (1-ms) duration, as shown schematically in Fig. 6(a), separated by 20-ms intervals. In order to record such short-period signals, we increase the camera frame rate to 3500 frames s^{-1} and the microwave modulation rate to 14 kHz, while still capturing 500 image frames, giving a 142-ms time series for each pixel covering a set of six applied pulses. We acquire $N = 2500$ repetitions of 500-frame-length image sets, extracting from this an average 500-frame-length time series for each pixel.

The relative strengths of the forward-current 1-ms pulses are shown in Fig. 6(b). As a consequence of the higher sensing bandwidth (higher frame rate), we capture more noise, giving a lower image SNR. We also note a reduction in the signal strength, which we attribute to a loss of modulation synchronicity between the camera and our microwave generator, arising from trigger incompatibility at modulation rates above approximately 3 kHz. Although this technical issue somewhat compromises the imaged signal strength, we clearly observe the applied pulsed signal in our magnetic field image, directly adjacent to the current-carrying track, indicated by a green arrow in Fig. 6(b).

The recorded magnetic field from the applied pulses is shown in the time series in Fig. 7, from (a) averaging all pixels with SNR > 3 and (b) for a single example pixel in the image on the circuit track. The 1-ms pulses can be clearly detected, with peak magnetic field amplitude 50 μT. Notably, detection is possible with SNR > 3 using data from just a single pixel receiving fluorescence from N-V centers directly adjacent to the circuit track. Although the signal is strongest along the current path, we can still observe the pulses within the images away from this region. This is demonstrated in Fig. 7(c), in which we plot the recorded time series for 20 000 pixels in a region

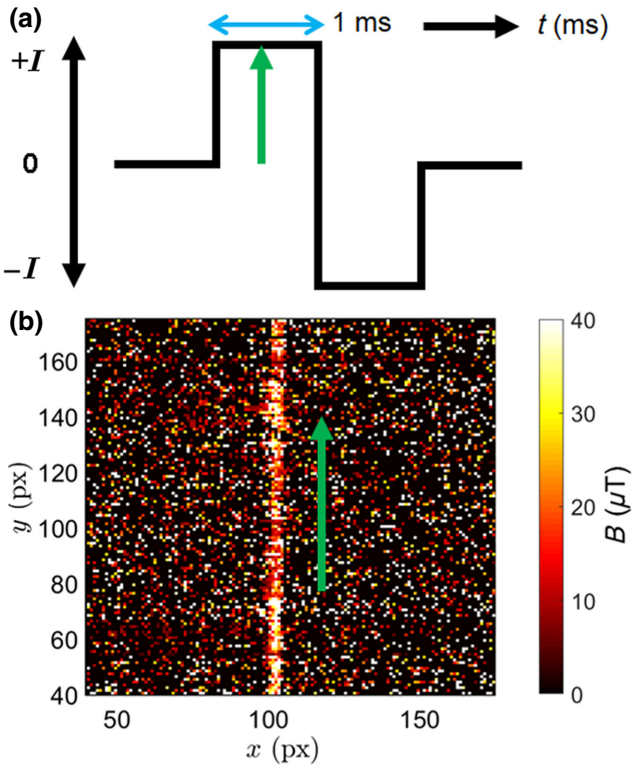

FIG. 6. (a) A schematic of the 1-ms (1-ms) forward- (reverse-) polarity pulsed-current signal. The signal is repeated every 20 ms. (b) An image map of the strength of the 1-ms forward component of the pulsed signal extracted from the pixel (px) time series over 500 frames (at 3500 frames s^{-1}), averaging the six pulses captured within the acquisition. For clarity, only pixel values with SNR > 3 are shown, with the remainder set to zero. The direction of the current through the cross circuit is indicated by a green arrow.

centered on the current track. Although having a lower SNR, the pulsed signal is still observable when imaging N-V center fluorescence up to a distance of at least 53 μm away from the current path.

D. Synthetic biosignal

Finally, we exemplify the acquisition of a biosignal with the same form as a neuronal signal, as may be found in the brain or nervous system of a living person or animal. We replicate the shape of a typical signal acquired from prior electrical recordings of fEPSPs in the hippocampus of a mouse [44–46], obtained from living dissected tissue slices (full details are given in the Supplemental Material [38]). We apply the signal using the AWG mode of our current source, with a maximum forward-current amplitude of 20 mA.

Note that this current is significantly higher in magnitude than the current generated by a signal in a real living neuron [47]. This is a necessity imposed by our suboptimal diamond, as the sensitivity that can be achieved

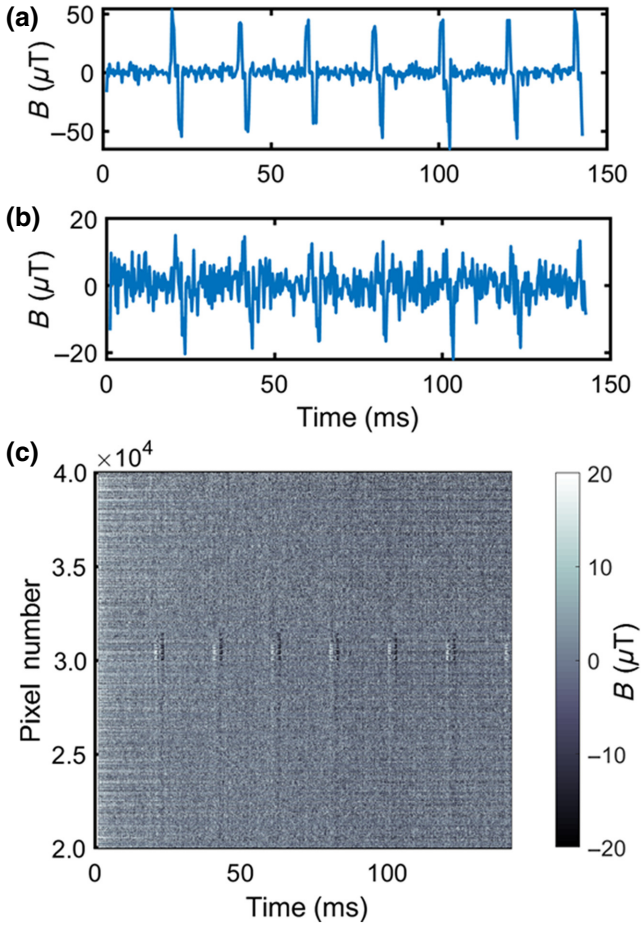

FIG. 7. The time series of the acquired signal for the acquisition period (142 ms at 3500 frames s^{-1}), taking the average over 1000 repeated 500-frame acquisitions. (a) The average of all pixels with SNR > 3, with the signal clearly resolved. (b) An example time series for a single pixel in a region of the image close to the current path, where despite the higher noise level, the signal can still be observed. (c) A sequence of time series for pixels 20 000–40 000, covering a region centered on the cross-current path. The strongest signal is observed for recording from pixels receiving fluorescence from N-V centers adjacent to the current-carrying track; however, the pulsed signal is still observable (with a decreasing SNR) away from it.

in our setup is short of that required to record the real biosignal. Our goal in this work is solely to demonstrate a method by which such a broadband signal (with frequency components from dc to kilohertz) could be accurately recovered in the time domain with simultaneous high-spatial-resolution imaging. We achieve this goal without trading spatial and temporal resolution, keeping both high enough to not only image signal propagation in, e.g., a neuronal network but to also record the signal shape, latency, and relative size, which are key for physiological study. The method we outline here is fully compatible with a more optimal diamond, in terms of a narrower ODMR line width, increased contrast, and a higher fluorescence emission up to the saturation limits of the camera.

The strength of the detected signal is demonstrated in Figs. 8(a) and 8(b), mirroring the equivalent Figs. 6 and 7 for the pulsed current, with the strongest signal again imaged closest to the current-carrying track. We extract the synthetic hippocampus signal from averaging the time series from $N = 2500 \times 500$ frame acquisitions for each pixel. A plot of this signal as compared to the applied-current signal can be seen in Fig. 9(a) for 5-pixel steps across the current track, shown as the blue dashed line in Fig. 8(b). In pixels recording fluorescence from N-V centers adjacent to the current track, we observe a strong signal, which is highly representative of the applied synthetic signal at a peak magnetic field strength of $15 - 20$ μT, with the signal decaying in strength in the image away from the current path. In Fig. 8(b), we plot the average signal acquired for all pixels with SNR > 3. This signal also replicates the applied current signal, as shown in the red dashed trace.

E. Noise scaling

A key feature that we note in all our data using the camera in lock-in mode is the constant reduction in noise with continual averaging, with a sensitivity consistently scaling as $1/\sqrt{N}$, where N is the number of acquired 500-frame image sets over which we average. We highlight that $1/\sqrt{N}$ scaling is extremely desirable for the acquisition of the regular repeating signals present in most biological or artificial systems, allowing far smaller signals to be temporally averaged and resolved than would be possible for a single 500-frame acquisition ($N = 1$, single-shot measurement). This scaling is demonstrated in Fig. 10(a), where we calculate the all-pixel average standard deviation of the magnetic field in the time series, taken with zero applied signal in a 5-ms period between the current pulses. After $N = 2500$ acquisitions, we reach a noise level of approximately 200 nT (4.78 nT $Hz^{-1/2}$ on a 1.75-kHz Nyquist-limited sensing bandwidth at 3500 frames s^{-1}), averaging over all 292×280 usable pixels in the image. A histogram of the noise on the individual pixels after 1000 acquisitions is given in Fig. 10(b), peaking at approximately $2.5 - 3$ μT. This corresponds to a per-pixel sensitivity of $59 - 71$ nT $Hz^{-1/2}$, or $295 - 355$ $\mu m^{3/2}$ $Hz^{-1/2}$, assuming that the pixels collect light from a $5 \times 5 \times 1$ μm sensing volume. The noise follows a Poisson distribution, as would be expected for an imaging system. The distribution is shifted toward the lower-sensitivity peak due to the nonuniform laser illumination of the diamond, the majority of pixels receiving a strong fluorescence signal, but one that drops off toward the edges of the field of view.

Note that in previous experiments using a conventional camera without lock-in capability, we have found the noise level to plateau at a relatively low number (N) of repeated

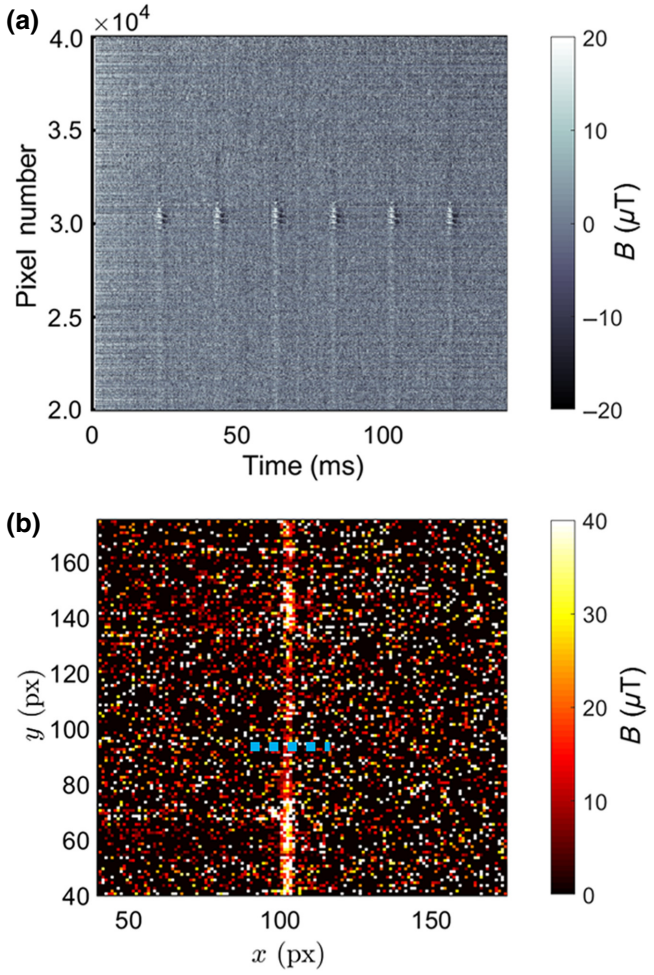

FIG. 8. The equivalent of the plots in Figs. 6 and 7 for the synthetic biosignal. As for the 1-ms pulses, the signal can be observed clearly for pixels (px) recording fluorescence from N-V centers directly adjacent to the current-carrying track but can also be observed at a lower SNR away from this region. The blue dashed line represents the track of pixels for the data presented in Fig. 9.

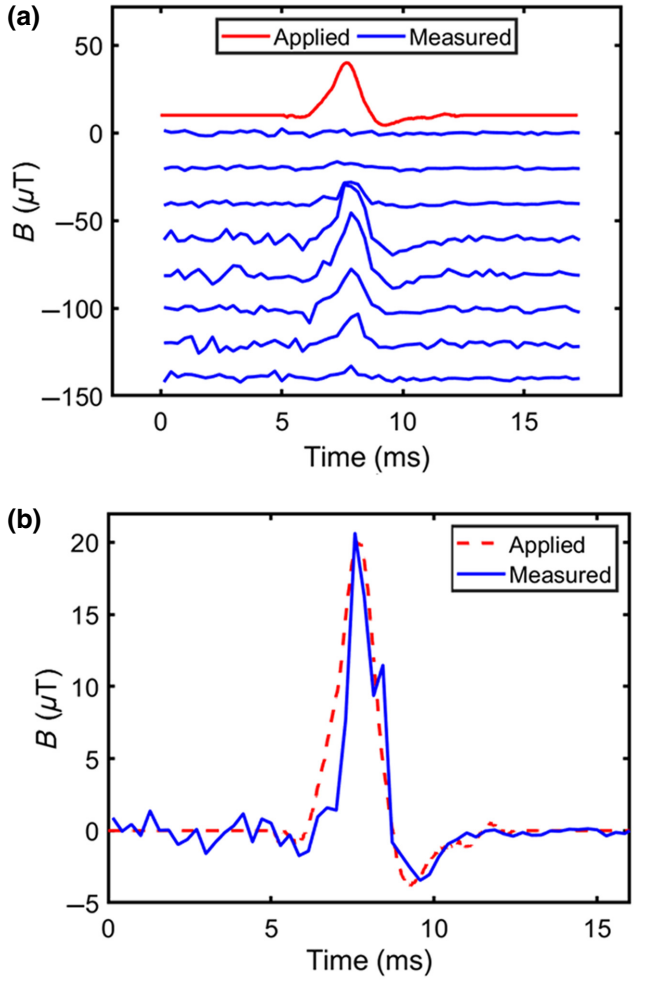

FIG. 9. (a) The magnetic field signal measured from individual pixels taking 5-pixel steps along the blue dashed line indicated in Fig. 8. For each step, we add an offset from the previous by -20 μT for clarity, with the (scaled) applied synthetic biosignal shown in red at the top. As expected, the signal is most clearly observed in the image region closest to the current path, dropping in strength to either side. (b) The signal recorded from averaging the response of all pixels with SNR > 3, overlaid onto the (scaled) generated signal (red, dashed). The signal recovered via the magnetic field imaging matches well with the applied signal, with no distortion or artifacts.

image acquisitions [29]. In Fig. 10, we demonstrate this effect by running the lock-in camera in intensity mode, where it functions as a conventional digital camera, with a signal proportional to the intensity of the fluorescence reaching each pixel. Here, we find that the noise reaches a plateau at around $3-4$ μT, with no further improvement possible by continued averaging. We attribute this behavior to the inclusion in the images of a high level of laser technical noise, predominantly as dc power fluctuations and in the range 10–25 kHz. When running in lock-in mode, the Helicam is able to perform common-mode rejection to eliminate a major part of this noise, across a frequency range of up to several hundred kilohertz when running at the maximum frame rate. Note that the $1/\sqrt{N}$ sensitivity scaling for the camera running in lock-in mode is the same as observed in our experiments using a common-mode noise-rejecting balanced photodetector [42]. The lock-in camera thus offers a unique capability to image and temporally resolve signals far below the single-shot sensitivity, which is not possible with a conventional digital camera.

F. Feasibility of biosignal recovery

In our experimental setup, it is necessary to apply a far larger synthetic biosignal current than would be realistically produced from neurons, permitting demonstration of the methodology for simultaneous spatial and temporal resolution of signals using a suboptimal diamond

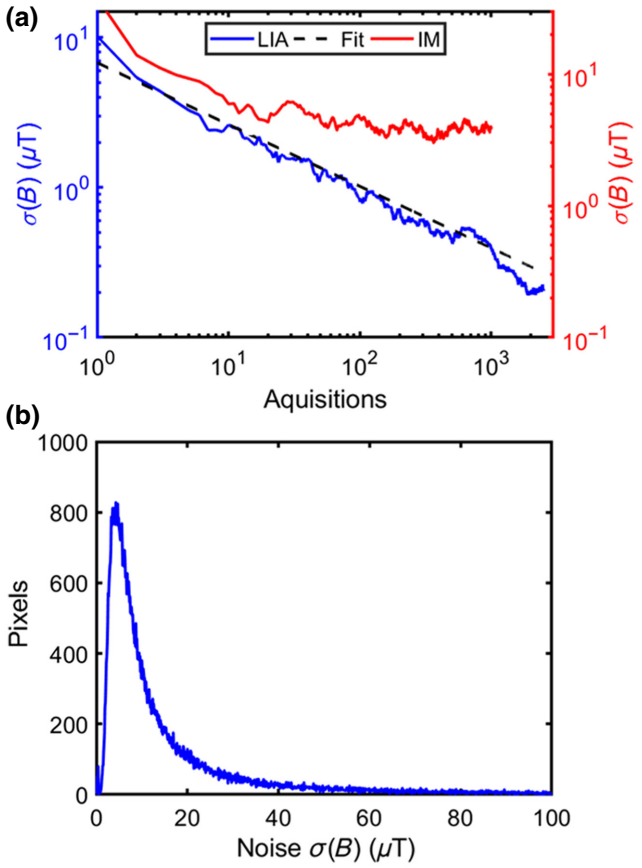

FIG. 10. (a) The scaling of the standard deviation $\sigma(B)$ of the magnetic field signal between the current pulses as a function of the number of 500-frame acquisitions N, as a measure of readout noise. We plot the performance of the camera running in lock-in mode (LIA) and running as a conventional digital camera in intensity mode (IM). In lock-in mode, the noise continually reduces, with a $1/\sqrt{N}$ trend. In intensity mode, the noise reaches a plateau at around 4 μT, with no further improvement by averaging. (b) The histogram of the individual pixel noise after 1000 acquisitions in lock-in mode, with the majority of pixels in the low-microtesla noise range.

and N-V ensemble. In this final section, we theoretically address the feasibility of performing the same measurements to recover a real biosignal, such as that from a tissue slice of a brain. We also consider this useful to more broadly highlight the sensitivity and feasibility limits for lock-in camera imaging using N-V centers for any applications.

Although we exemplify our technique using a signal shape as from neurons, there are many other biosignals covering a similar frequency range and bandwidth (but with higher amplitudes in the nanotesla range) that would be desirable to image and record using our technique. These include compound action potentials in muscle tissue, including from the heart, and in the central nervous system [48,49]. We could further enhance the biosignal strength by factors such as reducing the diamond-sample separation (the 10 μm in this work is suboptimal) or by designing a flux concentrator [50]. Also, our methodology is not limited to magnetic field sensing, being applicable to temperature and electric field sensing, where strong biosignals are also possible [51]. Previous theoretical calculations such as the works by Karadas *et al.* [52,53] have determined that neuronal signals of up to 1.5 nT are possible from neurons at a separation of > 50 μm between the diamond and the living tissue. For simplicity, we take an approximately 1 nT signal as our target minimum signal to resolve per pixel.

Our previous calculations in Wojciechowski *et al.* for cw-ODMR wide-field imaging [28] show that the minimum resolvable signal ΔB per pixel is linearly dependent on three parameters: the ODMR contrast C, the resonance line width Γ, and the SNR, assuming that optical shot noise dominates all other sources of noise, scaling as $\sqrt{P_{\mathrm{fl}}}$, where P_{fl} is the average total fluorescence power received by the camera imaging chip. Note that these factors are interrelated: for example, a higher N-V density will increase fluorescence emission but at the cost of a broader line width due to spin interaction between nitrogen dopants.

In order to define what is realistically achievable, we refer in Table I of the Supplemental Material [38] to parameters from published state-of-the-art experiments using a similar configuration, a millimeter-scale illumination area, and a cw methodology. For N-V densities in the low parts-per-million range, the collection of 1–10 mW of fluorescence per watt of pump-laser power, with a 0.6–1-MHz line width and up to 5% contrast, is achievable [42,43,54–56]. Note that these values represent a realistic picture from state-of-the-art experiments rather than a hard physical limit. Line widths down to 200 kHz and below have been realized [37,57] and although presently unfeasible for large N-V ensembles of many billions of N-V centers, an ODMR contrast of up to 30% has recently been realized in smaller ensembles through preferentially aligned growth [39,58,59].

We can calculate the resolvable signal level using realistic parameters, for an ODMR contrast $C = 5\%$, a resonance line width of 1 MHz, and a total $P_{\mathrm{fl}} = 1$ mW of fluorescence collected by all camera pixels (12 nW pixel^{-1}) on a field of view of approximately 1.5 mm. As in our previous work, we define the sensitivity of our recording in terms of the minimum signal ΔB per pixel that can be resolved per frame in each 500-frame acquisition. For these parameters, this is 360 nT pixel^{-1} (Table I), corresponding to a bandwidth-normalized level of 8.25 nT Hz$^{-1/2}$ pixel^{-1} when running at the maximum imaging frame rate of 3800 frames s^{-1}. For a pixel receiving light from a 1-μm-thick N-V layer in a 5×5 μm region in our image, this equates to a volume-normalized per-pixel level of 41.25 nT μm$^{3/2}$ Hz$^{-1/2}$, comparable to values used for biosensing [54]. Note that in this work,

we calculate our integrated per-frame noise using the Nyquist-limited sensing bandwidth on our 500-frame-per-pixel time series rather than the noise per imaging frame from averaging 3800 frames in a 1-s acquisition. Our ΔB-per-pixel values in this work thus differ by a factor of $\sqrt{2}$ for the same parameters ($C = 5\%$, $P_{\mathrm{fl}} = 1$ mW, and $\Gamma = 1$ MHz) as used in our earlier work [28].

A key advantage of running the camera in lock-in mode is that we are able to maximize utilization of the full well capacity (FWC) of the camera, as the camera reads and discharges the pixels at a much faster rate than the image frame rate (up to approximately 7 MHz) in order to perform lock-in demodulation. The camera can accept a far higher input optical power in lock-in mode as compared to intensity mode, as long as the number of photoelectrons generated per exposure time interval does not exceed the FWC. This equates to $P_{\mathrm{fl}} = 267$ mW at $f_{\mathrm{mod}} = 250$ kHz (0.14 μs exposure time), far higher than the 1 mW that would saturate the pixels running the camera in intensity mode (exposure time 1/3800 s). The difference between these operational modes is detailed further in the Supplemental Material [38]. Although it may be challenging to achieve this level of fluorescence in practice, for completeness we include the calculation at the FWC in Table I. Using the same realistic parameters for the diamond, this gives an improved per-image frame level of 161 nT pixel^{-1} at $P_{\mathrm{fl}} = 10$ mW, falling to 31 nT pixel^{-1} at $P_{\mathrm{fl}} = 267$ mW. We include this calculation so as not to preclude alternative sensing schemes that can direct more light into the camera, such as imaging the pump light absorption, or potentially exploiting future alternative defect centers with higher levels of optical emission.

Note that these values are calculated for the baseline Helicam model with a pixel optical fill factor of 6%. An updated model of the Helicam is available, fitted with pixel microlenses, which increase the pixel fill factor from 6% to $> 50\%$. Using pixel microlenses, the camera can achieve the same sensitivity at, approximately, a factor of 10 less input fluorescence power (Table I). As our imaging is performed on axis using a flat-substrate diamond, with little need to accept light arriving at oblique angles, such microlenses are suitable for the N-V imaging methods that we outline here.

The sensitivity values defined so far are only applicable to a single-shot measurement (a single 500-frame acquisition, $N = 1$) of a single repetition ($N_s = 1$) of the biosignal. As we show in Fig. 10, multiple acquisitions ($N > 1$) can be averaged to reduce the noise and recover a signal of 1 nT or below. The extraction, comparison, and averaging of time-synchronized signal repetitions is an extensively used technique in biophysics (epoching), for electrical and magnetic recording, including for bulk–N-V–center recording, where it has been demonstrated that signals can be recorded from living specimens kept alive *in vitro* for many hours [42,54]. This approach is made possible by the stable nature of wide classes of biosignals, which by necessity retain a consistent shape and amplitude on repeated stimulation. As we detail in the previous section, a key advantage of the lock-in camera is that it allows clear $1/\sqrt{N}$ scaling of the averaged noise floor, without reaching a plateau as observed using a conventional camera lacking common-mode rejection of laser technical noise.

Furthermore, many repetitions of the same biosignal ($N_s > 1$) can be stimulated within each 500-frame acquisition. For neuronal action potentials, this can be at rates of up to a few hundred hertz [53,62]. For 100-Hz signal repetitions at 3500 frames s^{-1}, it is possible to capture $N_s = 14$ repetitions in each 500-frame acquisition. For the camera working at the physical FWC limit in Table I that requires $N = 485$ to resolve a signal of 1 nT pixel^{-1}, this level could be reached in just $N = 485/14 = 35$ acquisitions.

As we demonstrate in the previous sections, acquisitions of $N = 2500$ over several hours are more than feasible. The primary limitation on averaging, as detailed in Table I and in Fig. 14 of the Supplemental Material [38], is the USB 2.0 transfer time between the camera and the PC. Assuming the immediate availability of image frames after capture, by using the GigE interface standard over Ethernet for high-bandwidth data transmission, this transfer time could be reduced to a few tens of milliseconds. This would allow the acquisition of significantly more averages in far less time, minimizing the noise and reaching the signal level in minutes rather than hours of image capture.

In the work that we present here, we are far from the ideal diamond parameters discussed in our previous work, with a relatively broad line width (approximately 2.3 MHz) and ODMR contrast (1.2–1.6%). To generate sufficient contrast, it is also necessary to supply a relatively high microwave power (approximately 40 dBm), meaning that we cannot resolve the ^{15}N hyperfine resonances in the ODMR spectrum due to power broadening [63]. Although the fluorescence emission of our diamond is intrinsically poor (a maximum of 152 μW full sensor or 1.7 nW pixel^{-1}), we purposely compromise this further in our experiment by spreading the pump laser over as much of the imaging region as possible to realize a desirable large field of view. Although a modest reduction of the sensing area could improve the sensitivity, by focusing the pump laser and using a higher magnification and a higher-numerical-aperture objective, N-V charge-state effects would limit the benefit of this approach toward the limit of higher intensity [64]. Based on our diamond parameters, we calculate that we can resolve, at minimum, a signal of 4.55 μT pixel^{-1} (104 nT Hz$^{-1/2}$ pixel^{-1} or 232 nT μm$^{3/2}$ Hz$^{-1/2}$ pixel^{-1}), far short of the necessary sensitivity for neuronal signal recovery but sufficient for many other applications, including integrated circuit imaging. Note that this is higher than our measured median

TABLE I. The minimum per-pixel resolvable signal ΔB in $\mathrm{pT\,Hz^{-1/2}}$ and integrated over one image frame in nanotesla for the Helicam running at 3800 frames $\mathrm{s^{-1}}$ in lock-in mode. The calculations are based on the methodology detailed in Wojciechowski *et al.* [28]. We vary the ODMR contrast (C, %), the line width (Γ, MHz), the total fluorescence power at the camera (P_{fl}, mW), and pixel full well capacity (FWC). All values are for a single signal repetition ($N_s = 1$) in a 500-frame acquisition. We also estimate the number of 500-frame acquisitions (N) to reach per-frame noise floors of 1 $\mathrm{nT\,pixel^{-1}}$ and 50 $\mathrm{pT\,pixel^{-1}}$ based on $\sqrt{(N)}$ SNR scaling and the time (t) to reach N by transfer over USB 2.0 and over Ethernet using GigE. Each of the pixels images a 5×5 $\mu\mathrm{m}^2$ area on a field of view of approximately 1.5×1.5 mm^2.

Parameters	C (%)	Γ (MHz)	P_{fl} (mW)	ΔB per pixel per frame $N = 1$ ($\mathrm{pT\,Hz^{-1/2}}$)	ΔB per pixel per frame $N = 1$ (nT)	Number N acquired to 1 nT	Number N acquired to 50 pT	Time t to 1 nT USB 2.0 (h)	Time t to 1 nT GigE (min)
This work From Ref. [28]	1.2	4	0.152	(104 nT)	(4.55 μT)	2.07×10^7	4.29×10^9	(>week)	(>week)
$P_{\mathrm{fl}} = 1$ mW	5	1	1	8 250	360	1.29×10^5	5.18×10^7	259	284
$P_{\mathrm{fl}} =$ 10 mW	5	1	10	2 610	113.8	12 962	5.18×10^6	25.9	28.4
$P_{\mathrm{fl}} =$ 100 mW	5	1	100	826	36	1 296	5.18×10^5	2.59	2.84
FWC limit[a]	5	1	267	505	22	485	1.94×10^5	0.97	1.06
Optimal Γ	5	0.2	267	101	4.43	20	7 854	(2.4 min)	(2.63 s)
Optimal Γ, C	30	0.2	267	42	1.81	3	1 309	(36 s)	(< 1 s)
With microlenses[b]	5	0.2	24	101	4.43	20	7 854	(2.4 min)	(2.63 s)

[a]Physical FWC reached in a single internal frame (1×10^6 frames $\mathrm{s^{-1}}$ at < 250 kHz modulation).
[b]Increases optical fill factor to > 50% from 6%.

value of 2.91 $\mu\mathrm{T\,pixel^{-1}}$ (Fig. 10), as our calculations are based on only an even power distribution over all pixels.

We highlight that although we do not at this time have the diamond to reach the necessary levels of sensitivity for recovery of real neuronal signals, no aspect of the measurement method utilizing the lock-in camera is incompatible with future material improvement, including visible-wavelength color centers in nondiamond materials (e.g., SiC [65]). In Table I, we estimate the minimum resolvable field based on a range of optimal diamond parameters, showing that a single-shot minimum detectable field ($N = 1$) in the low-nanotesla-per-pixel range can be reached, with a time-averaged noise floor ($N > 1$) in the tens-of-picotesla-per-pixel range within a reasonable number of image acquisitions.

IV. CONCLUSIONS

In this work, we demonstrate proof-of-principle passive and remote imaging of propagating electrical current in a circuit, using a lock-in amplifier camera. We image the induced magnetic field produced by the current in the circuit via variations in the fluorescence emission from N-V centers in diamond. Using a simple cw method, we demonstrate (micrometer-scale) high spatial resolution with wide (millimeter-scale) field-of-view imaging with simultaneous spatially resolved temporal resolution of magnetic field signals up to kilohertz frequencies. We demonstrate broadband recovery of these signals, covering the dc to kilohertz range, which is key to accurately recording the signal shape, latency, and relative amplitudes without aliasing or undersampling. We exemplify our method using single-frequency ac signals (as are typical in electrical-power-distribution systems), a rapidly pulsed current (as is typical in integrated circuits), and a representation of a biosignal (as generated in the living brain). We show that significantly faster real current and magnetic field signals can be resolved than previously achieved in the literature (3800 frames $\mathrm{s^{-1}}$ per 1.75 kHz signal-recovery bandwidth up to the Nyquist frequency is possible).

We emphasize the importance of the $1/\sqrt{N}$ scaling of the sensitivity with continual averaging using the Helicam, which enables the recovery of far smaller signals well below the single-shot-measurement noise limit. This is a significant advantage of the lock-in camera over conventional cameras, where dc and laser technical noise can cause the sensitivity to plateau after a relatively low number of acquisitions (around $3-4$ $\mu\mathrm{T\,pixel^{-1}}$). We consider this feature to be particularly useful in either mapping repeated consistent fast signals such as electrical transport or magnetism in two-dimensional materials [32], for wide classes of repeating biosignals including

neuronal action potentials or for slowly varying long-period measurements, such as temperature sensing.

The method that we demonstrate can be readily adapted to a typical inverted-microscope setup used for N-V sensing and imaging [42,54]. We detail how sufficient sensitivity to recover real biosignals could be obtained with reference to our previous work on lock-in camera sensitivity [28]. Although our diamond does not allow us to reach these necessary levels of sensitivity, we detail a clear path of improvements in material growth and optimization that could reach a sufficient level. The methods that we demonstrate here are fully compatible with these advances and represent a clear means by which such signals could be resolved. The potential for implementation of pulsed laser and microwave protocols, recently demonstrated by Hart *et al.* [66], also offers an even greater possibility to increase the sensitivity beyond the cw method.

Although pulsed measurement offers the prospect of greater sensitivity, we consider that the cw method may be of use for applications where there is a large degree of variation in the laser or microwave drive fields and/or intrinsic diamond parameters. One such example is wide-field imaging of multiple nanodiamonds in a single field of view; for example, as temperature probes in cells [67]. For such an application, it will be challenging to apply microwave and laser pulses of the right power and length to correctly interrogate every N-V in diamonds scattered across a wide field of view. The use of the cw method with the lock-in camera would avoid this problem, recovering the ODMR and any temperature and/or magnetic field measurement for all nanodiamonds simultaneously.

We highlight that our method allows the full resolution of ODMR spectra and key parameters for the N-V centers for each pixel, across a field of view far wider than the tens of micrometers typical in the literature. This capability to recover the per-pixel ODMR allows us to precisely measure inhomogeneities in, e.g., laser power or resonance detuning across the image, while also ensuring that any effect across the image remains within our sensing dynamic range (on the ODMR slope and magnetically sensitive). In this work, this enables nonuniform laser illumination at the Brewster angle for diamond, enhancing the coupling of pump light into the diamond and boosting the sensitivity. This capability offers significant benefits over the common technique in the literature of imaging with pump excitation through the microscope objective, in terms of greater fluorescence emission, a wider field of view, and no saturation of contrast. As the sensitivity plateaus as a function of repeated averages N as detailed above, a conventional camera cannot easily recover the per-pixel ODMR, thus demanding a restricted highly homogeneous imaging region in terms of the laser and microwave fields and the N-V contrast and detuning. The lock-in camera thus enables the wide millimeter-scale field of view necessary to study signal propagation in biological neuronal networks or to map current paths in integrated circuits for fault detection.

By extracting the time-domain data from each camera pixel using our lock-in camera, we can apply time- and frequency-domain noise-filtering methods that are key for recovering signals in bulk-diamond-sensing experiments [29,42]. In particular, this allows the elimination of stationary noise such as 50/150 Hz mains and higher harmonics and nonstationary noise from pumps and ventilation in each pixel. This is a significantly stronger source of noise than from diamond material inhomogeneity or from camera-measurement electronics noise, with the 50-Hz signal of approximately $200 - 400$ nT due to ordinary building mains cabling. This capability is vital for future weak-signal acquisition, particularly for applications in an ordinary laboratory or clinical environment without extensive and costly magnetic shielding.

Note that a disadvantage of our method is that we split our N-V resonances, which means that we are only sensitive in one particular direction at a time. This results in the component of the field measured being much less than the absolute magnitude of the vector magnetic field, i.e., if we are most sensitive in z and the field is mostly in (x,y), we will only record a weak component of the field. We model this aspect (full details are given in the Supplemental Material [38]), matching experimental observations. This disadvantage can be overcome by adjusting the sample geometry to align the sensitive axis along the direction corresponding to the maximum target signal. This is a method that we employ in bulk-sensing experiments with additional contrast and sensitivity gained by resonance overlap through offset field alignment along the diamond crystallographic [110] direction. Alternatively, it is possible to select between N-V axes, by shifting the microwave frequency to another resonance. Via rapid sequential switching, this could also provide vector sensing, which would be the ultimate solution to recover all components of the vector magnetic field. There are, however, further complexities that must be overcome to achieve this, including the loss of sensing bandwidth due to the finite microwave-frequency switching time and calibration of the translation between the resonance shift and the field amplitude in each axis.

ACKNOWLEDGMENTS

The work presented here was mainly funded by the Novo Nordisk Foundation through the bioQ project. It also received partial funding by the Danish National Research Foundation (DNRF) through the Centre for Macroscopic Quantum States (bigQ, DNRF0142), the Novo Nordisk Foundation through the "Ultra-sensitive bio-magnetometers with macro to nano resolution" (BIOMAG) and QuantBioEng projects, the EMPIR program

cofinanced by the Participating States, and from the European Union Horizon 2020 research and innovation program via the "Quantum sensors for metrology based on single-atom-like device technology" (QADeT) program (20IND05). We acknowledge Kristian Hagsted Rasmussen for assistance with microfabrication.

Note added.—Recently, we have been informed by the camera manufacturer that by activating an offset compensation circuit to eliminate more of the unmodulated dc photocurrent as the camera collects fluorescence in lock-in mode [60], we can achieve an *effective* FWC a factor of 30 higher (1.05×10^7) than the physical value, allowing a theoretical maximum input power in lock-in mode of $P_{\mathrm{fl}} \approx 4.6$ W or at least up to the (unmeasured) camera damage threshold [61]. This can be used to remove the well-capacity constraint, such that the sensitivity is only constrained by the amount of fluorescence generated by the N-V centers. We have also become aware of contemporary work by Parashar *et al.* [68], independently following a similar procedure as we outline in this work, temporally (but not spatially) resolving ac signals from a bulk magnetic field applied across the diamond using a field coil rather than a microcircuit. We have also become aware of the contemporary work by Turner [69], again following a similar procedure with a lock-in camera to achieve high spatial resolution of low single-frequency alternating current in phantom circuits. These works and ours highlight the key advantages of the simplicity of the technique based on the lock-in camera technique and the limitations, particularly in terms of the possibility of attaining significantly higher sensitivity through improved diamond growth and irradiation.

[1] R. Hoffmann-Vogel, Electromigration and the structure of metallic nanocontacts, Appl. Phys. Rev. **4**, 031302 (2017).
[2] U. Kindereit, in *2014 IEEE International Reliability Physics Symposium* (IEEE, 2014).
[3] K. Nakamae, Electron microscopy in semiconductor inspection, Meas. Sci. Technol. **32**, 052003 (2021).
[4] J. True, C. Xi, N. Jessurun, K. Ahi, and N. Asadizanjani, Review of THz-based semiconductor assurance, Opt. Eng. **60**, 060901 (2021).
[5] A. V. Ulyanova, C. Cottone, C. D. Adam, K. G. Gagnon, D. K. Cullen, T. Holtzman, B. G. Jamieson, P. F. Koch, H. I. Chen, V. E. Johnson, and J. A. Wolf, Multichannel silicon probes for awake hippocampal recordings in large animals, Front. Neurosci. **13**, (2019).
[6] K. Ohki, S. Chung, Y. H. Ch'ng, P. Kara, and R. C. Reid, Functional imaging with cellular resolution reveals precise micro-architecture in visual cortex, Nature **433**, 597 (2005).
[7] F. Dolde, H. Fedder, M. W. Doherty, T. Nöbauer, F. Rempp, G. Balasubramanian, T. Wolf, F. Reinhard, L. C. L. Hollenberg, F. Jelezko, and J. Wrachtrup, Electric-field sensing using single diamond spins, Nat. Phys. **7**, 459 (2011).
[8] P. Neumann, I. Jakobi, F. Dolde, C. Burk, R. Reuter, G. Waldherr, J. Honert, T. Wolf, A. Brunner, J. H. Shim, D. Suter, H. Sumiya, J. Isoya, and J. Wrachtrup, High-precision nanoscale temperature sensing using single defects in diamond, Nano Lett. **13**, 2738 (2013).
[9] S. Knauer, J. P. Hadden, and J. G. Rarity, In-situ measurements of fabrication induced strain in diamond photonic-structures using intrinsic colour centres, npj Quantum Inf. **6**, 50 (2020).
[10] D. Cohen, R. Nigmatullin, O. Kenneth, F. Jelezko, M. Khodas, and A. Retzker, Utilising NV based quantum sensing for velocimetry at the nanoscale, Sci. Rep. **10**, 5298 (2020).
[11] Y. Liu, H. Guo, W. Zhang, Z. Zhang, Z. Li, Y. Li, J. Tang, Z. Ma, and J. Liu, Nanoscale detection of faint machinery vibration using the NV center in diamond, Phys. Lett. A **384**, 126832 (2020).
[12] J. M. Taylor, P. Cappellaro, L. Childress, L. Jiang, D. Budker, P. R. Hemmer, A. Yacoby, R. Walsworth, and M. D. Lukin, High-sensitivity diamond magnetometer with nanoscale resolution, Nat. Phys. **4**, 810 (2008).
[13] S. Hong, M. S. Grinolds, L. M. Pham, D. L. Sage, L. Luan, R. L. Walsworth, and A. Yacoby, Nanoscale magnetometry with NV centers in diamond, MRS Bull. **38**, 155 (2013).
[14] T. Wolf, P. Neumann, K. Nakamura, H. Sumiya, T. Ohshima, J. Isoya, and J. Wrachtrup, Subpicotesla diamond magnetometry, Phys. Rev. X **5**, 041001 (2015).
[15] A. Gruber, Scanning confocal optical microscopy and magnetic resonance on single defect centers, Science **276**, 2012 (1997).
[16] P. Delaney, J. C. Greer, and J. A. Larsson, Spin-polarization mechanisms of the nitrogen-vacancy center in diamond, Nano Lett. **10**, 610 (2010).
[17] E. V. Levine, M. J. Turner, P. Kehayias, C. A. Hart, N. Langellier, R. Trubko, D. R. Glenn, R. R. Fu, and R. L. Walsworth, Principles and techniques of the quantum diamond microscope, Nanophotonics **8**, 1945 (2019).
[18] A. Horsley, P. Appel, J. Wolters, J. Achard, A. Tallaire, P. Maletinsky, and P. Treutlein, Microwave Device Characterization Using a Widefield Diamond Microscope, Phys. Rev. Appl. **10**, 044039 (2018).
[19] Y. Chen, Z. Li, H. Guo, D. Wu, and J. Tang, Simultaneous imaging of magnetic field and temperature using a wide-field quantum diamond microscope, EPJ Quantum Technol. **8**, 8 (2021).
[20] J.-P. Tetienne, N. Dontschuk, D. A. Broadway, A. Stacey, D. A. Simpson, and L. C. L. Hollenberg, Quantum imaging of current flow in graphene, Sci. Adv. **3**, e1602429 (2017).
[21] M. J. H. Ku, T. X. Zhou, Q. Li, Y. J. Shin, J. K. Shi, C. Burch, L. E. Anderson, A. T. Pierce, Y. Xie, A. Hamo, U. Vool, H. Zhang, F. Casola, T. Taniguchi, K. Watanabe, M. M. Fogler, P. Kim, A. Yacoby, and R. L. Walsworth, Imaging viscous flow of the Dirac fluid in graphene, Nature **583**, 537 (2020).
[22] D. R. Glenn, R. R. Fu, P. Kehayias, D. L. Sage, E. A. Lima, B. P. Weiss, and R. L. Walsworth, Micrometer-scale magnetic imaging of geological samples using a quantum diamond microscope, Geochem. Geophys. Geosyst. **18**, 3254 (2017).
[23] J. C. Price, R. Mesquita-Ribeiro, F. Dajas-Bailador, and M. L. Mather, Widefield, spatiotemporal mapping of

spontaneous activity of mouse cultured neuronal networks using quantum diamond sensors, Front. Phys. **8**, (2020).

[24] D. L. Sage, K. Arai, D. R. Glenn, S. J. DeVience, L. M. Pham, L. Rahn-Lee, M. D. Lukin, A. Yacoby, A. Komeili, and R. L. Walsworth, Optical magnetic imaging of living cells, Nature **496**, 486 (2013).

[25] R. Schirhagl, K. Chang, M. Loretz, and C. L. Degen, Nitrogen-vacancy centers in diamond: Nanoscale sensors for physics and biology, Annu. Rev. Phys. Chem. **65**, 83 (2014).

[26] L. T. Hall, G. C. G. Beart, E. A. Thomas, D. A. Simpson, L. P. McGuinness, J. H. Cole, J. H. Manton, R. E. Scholten, F. Jelezko, J. Wrachtrup, S. Petrou, and L. C. L. Hollenberg, High spatial and temporal resolution wide-field imaging of neuron activity using quantum NV-diamond, Sci. Rep. **2**, 401 (2012).

[27] L. M. Pham, D. L. Sage, P. L. Stanwix, T. K. Yeung, D. Glenn, A. Trifonov, P. Cappellaro, P. R. Hemmer, M. D. Lukin, H. Park, A. Yacoby, and R. L. Walsworth, Magnetic field imaging with nitrogen-vacancy ensembles, New J. Phys. **13**, 045021 (2011).

[28] A. M. Wojciechowski, M. Karadas, A. Huck, C. Osterkamp, S. Jankuhn, J. Meijer, F. Jelezko, and U. L. Andersen, Contributed review: Camera-limits for wide-field magnetic resonance imaging with a nitrogen-vacancy spin sensor, Rev. Sci. Instrum. **89**, 031501 (2018).

[29] J. L. Webb, L. Troise, N. W. Hansen, J. Achard, O. Brinza, R. Staacke, M. Kieschnick, J. Meijer, J.-F. Perrier, K. Berg-Sørensen, A. Huck, and U. L. Andersen, Optimization of a diamond nitrogen vacancy centre magnetometer for sensing of biological signals, Front. Phys. **8**, (2020).

[30] R. Tanos, W. Akhtar, S. Monneret, F. F. de Oliveira, G. Seniutinas, M. Munsch, P. Maletinsky, L. le Gratiet, I. Sagnes, A. Dréau, C. Gergely, V. Jacques, G. Baffou, and I. Robert-Philip, Optimal architecture for diamond-based wide-field thermal imaging, AIP Adv. **10**, 025027 (2020).

[31] D. A. Simpson, J.-P. Tetienne, J. M. McCoey, K. Ganesan, L. T. Hall, S. Petrou, R. E. Scholten, and L. C. L. Hollenberg, Magneto-optical imaging of thin magnetic films using spins in diamond, Sci. Rep. **6**, 22797 (2016).

[32] D. A. Broadway, S. C. Scholten, C. Tan, N. Dontschuk, S. E. Lillie, B. C. Johnson, G. Zheng, Z. Wang, A. R. Oganov, S. Tian, C. Li, H. Lei, L. Wang, L. C. L. Hollenberg, and J.-P. Tetienne, Imaging domain reversal in an ultrathin van der Waals ferromagnet, Adv. Mater. **32**, 2003314 (2020).

[33] Z. Kazi, I. M. Shelby, H. Watanabe, K. M. Itoh, V. Shutthanandan, P. A. Wiggins, and K.-M. C. Fu, Wide-Field Dynamic Magnetic Microscopy Using Double-Double Quantum Driving of a Diamond Defect Ensemble, Phys. Rev. Appl. **15**, 054032 (2021).

[34] K. Mizuno, H. Ishiwata, Y. Masuyama, T. Iwasaki, and M. Hatano, Simultaneous wide-field imaging of phase and magnitude of AC magnetic signal using diamond quantum magnetometry, Sci. Rep. **10**, 11611 (2020).

[35] P. Lambelet, in *Optical Measurement Systems for Industrial Inspection VII*, edited by P. H. Lehmann, W. Osten, and K. Gastinger (SPIE, 2011).

[36] R. Patel, S. Achamfuo-Yeboah, R. Light, and M. Clark, Widefield heterodyne interferometry using a custom CMOS modulated light camera, Opt. Express **19**, 24546 (2011).

[37] J. F. Barry, J. M. Schloss, E. Bauch, M. J. Turner, C. A. Hart, L. M. Pham, and R. L. Walsworth, Sensitivity optimization for NV-diamond magnetometry, Rev. Mod. Phys. **92**, 015004 (2020).

[38] See the Supplemental Material at http://link.aps.org/supplemental/10.1103/PhysRevApplied.17.064051 for supplementary data and plots referred to in the text.

[39] L. M. Pham, N. Bar-Gill, D. L. Sage, C. Belthangady, A. Stacey, M. Markham, D. J. Twitchen, M. D. Lukin, and R. L. Walsworth, Enhanced metrology using preferential orientation of nitrogen-vacancy centers in diamond, Phys. Rev. B **86**, (2012).

[40] N. D. Lai, D. Zheng, F. Jelezko, F. Treussart, and J.-F. Roch, Influence of a static magnetic field on the photoluminescence of an ensemble of nitrogen-vacancy color centers in a diamond single-crystal, Appl. Phys. Lett. **95**, 133101 (2009).

[41] A. Cooper, E. Magesan, H. N. Yum, and P. Cappellaro, Time-resolved magnetic sensing with electronic spins in diamond, Nat. Commun. **5**, 3141 (2014).

[42] J. L. Webb, L. Troise, N. W. Hansen, C. Olsson, A. M. Wojciechowski, J. Achard, O. Brinza, R. Staacke, M. Kieschnick, J. Meijer, A. Thielscher, J.-F. Perrier, K. Berg-Sørensen, A. Huck, and U. L. Andersen, Detection of biological signals from a live mammalian muscle using an early stage diamond quantum sensor, Sci. Rep. **11**, 2412 (2021).

[43] J. M. Schloss, J. F. Barry, M. J. Turner, and R. L. Walsworth, Simultaneous Broadband Vector Magnetometry Using Solid-State Spins, Phys. Rev. Appl. **10**, (2018).

[44] C. Henneberger, T. Papouin, S. H. R. Oliet, and D. A. Rusakov, Long-term potentiation depends on release of D-serine from astrocytes, Nature **463**, 232 (2010).

[45] R. L. Redondo, H. Okuno, P. A. Spooner, B. G. Frenguelli, H. Bito, and R. G. M. Morris, Synaptic tagging and capture: Differential role of distinct calcium/calmodulin kinases in protein synthesis-dependent long-term potentiation, J. Neurosci. **30**, 4981 (2010).

[46] I. Sánchez-Rodríguez, S. Temprano-Carazo, A. Nájera, S. Djebari, J. Yajeya, A. Gruart, J. M. Delgado-García, L. Jiménez-Díaz, and J. D. Navarro-López, Activation of G-protein-gated inwardly rectifying potassium (Kir3/GirK) channels rescues hippocampal functions in a mouse model of early amyloid-β pathology, Sci. Rep. **7**, (2017).

[47] J. Mitterdorfer and B. P. Bean, Potassium currents during the action potential of hippocampal CA3 neurons, J. Neurosci. **22**, 10106 (2002).

[48] W. D. Arnold, K. A. Sheth, C. G. Wier, J. T. Kissel, A. H. Burghes, and S. J. Kolb, Electrophysiological motor unit number estimation (MUNE) measuring compound muscle action potential (CMAP) in mouse hindlimb muscles, J. Vis. Exp. (2015),.

[49] K. Arai, A. Kuwahata, D. Nishitani, I. Fujisaki, R. Matsuki, Z. Xin, Y. Nishio, X. Cao, Y. Hatano, S. Onoda, C. Shinei, M. Miyakawa, T. Taniguchi, M. Yamazaki, T. Teraji, T. Ohshima, M. Hatano, M. Sekino, and T. Iwasaki, Millimetre-scale magnetocardiography of living rats using a solid-state quantum sensor (2021), ArXiv:2105.11676.

[50] I. Fescenko, A. Jarmola, I. Savukov, P. Kehayias, J. Smits, J. Damron, N. Ristoff, N. Mosavian, and V. M. Acosta, Diamond magnetometer enhanced by ferrite flux concentrators, Phys. Rev. Res. **2**, 023394 (2020).

[51] A. M. Romshin, V. Zeeb, A. K. Martyanov, O. S. Kudryavtsev, D. G. Pasternak, V. S. Sedov, V. G. Ralchenko, A. G. Sinogeykin, and I. I. Vlasov, A new approach to precise mapping of local temperature fields in submicrometer aqueous volumes, Sci. Rep. **11**, 14228 (2021).

[52] M. Karadas, A. M. Wojciechowski, A. Huck, N. O. Dalby, U. L. Andersen, and A. Thielscher, Feasibility and resolution limits of opto-magnetic imaging of neural network activity in brain slices using color centers in diamond, Sci. Rep. **8**, 4503 (2018).

[53] M. Karadas, C. Olsson, N. W. Hansen, J.-F. Perrier, J. L. Webb, A. Huck, U. L. Andersen, and A. Thielscher, *In-vitro* recordings of neural magnetic activity from the auditory brainstem using color centers in diamond: A simulation study, Front. Neurosci. **15**, (2021).

[54] J. F. Barry, M. J. Turner, J. M. Schloss, D. R. Glenn, Y. Song, M. D. Lukin, H. Park, and R. L. Walsworth, Optical magnetic detection of single-neuron action potentials using quantum defects in diamond, Proc. Nat. Acad. Sci. **113**, 14133 (2016).

[55] H. Clevenson, M. E. Trusheim, C. Teale, T. Schröder, D. Braje, and D. Englund, Broadband magnetometry and temperature sensing with a light-trapping diamond waveguide, Nat. Phys. **11**, 393 (2015).

[56] H. Yu, Y. Xie, Y. Zhu, X. Rong, and J. Du, Enhanced sensitivity of the nitrogen-vacancy ensemble magnetometer via surface coating, Appl. Phys. Lett. **117**, 204002 (2020).

[57] E. E. Kleinsasser, M. M. Stanfield, J. K. Q. Banks, Z. Zhu, W.-D. Li, V. M. Acosta, H. Watanabe, K. M. Itoh, and K.-M. C. Fu, High density nitrogen-vacancy sensing surface created via He^{+} ion implantation of ^{12}C diamond, Appl. Phys. Lett. **108**, 202401 (2016).

[58] C. Osterkamp, M. Mangold, J. Lang, P. Balasubramanian, T. Teraji, B. Naydenov, and F. Jelezko, Engineering preferentially-aligned nitrogen-vacancy centre ensembles in CVD grown diamond, Sci. Rep. **9**, (2019).

[59] P. Balasubramanian, C. Osterkamp, Y. Chen, X. Chen, T. Teraji, E. Wu, B. Naydenov, and F. Jelezko, dc magnetometry with engineered nitrogen-vacancy spin ensembles in diamond, Nano Lett. **19**, 6681 (2019).

[60] J. Schloss, Ph.D. thesis, Department of Physics, Massachusetts Institute of Technology, 2019.

[61] Heliotis, Private communication (2021).

[62] B. Wang, W. Ke, J. Guang, G. Chen, L. Yin, S. Deng, Q. He, Y. Liu, T. He, R. Zheng, Y. Jiang, X. Zhang, T. Li, G. Luan, H. D. Lu, M. Zhang, X. Zhang, and Y. Shu, Firing frequency maxima of fast-spiking neurons in human, monkey, and mouse neocortex, Front. Cell. Neurosci. **10**, (2016).

[63] A. Dréau, M. Lesik, L. Rondin, P. Spinicelli, O. Arcizet, J.-F. Roch, and V. Jacques, Avoiding power broadening in optically detected magnetic resonance of single NV defects for enhanced dc magnetic field sensitivity, Phys. Rev. B **84**, 195204 (2011).

[64] S. T. Alsid, J. F. Barry, L. M. Pham, J. M. Schloss, M. F. O'Keeffe, P. Cappellaro, and D. A. Braje, Photoluminescence Decomposition Analysis: A Technique to Characterize N-*V* Creation In Diamond, Phys. Rev. Appl. **12**, 044003 (2019).

[65] S. Castelletto and A. Boretti, Silicon carbide color centers for quantum applications, J. Phys.: Photon. **2**, 022001 (2020).

[66] C. A. Hart, J. M. Schloss, M. J. Turner, P. J. Scheidegger, E. Bauch, and R. L. Walsworth, N-*V*–Diamond Magnetic Microscopy Using a Double Quantum 4-Ramsey Protocol, Phys. Rev. Appl. **15**, 044020 (2021).

[67] M. Fujiwara, S. Sun, A. Dohms, Y. Nishimura, K. Suto, Y. Takezawa, K. Oshimi, L. Zhao, N. Sadzak, Y. Umehara, Y. Teki, N. Komatsu, O. Benson, Y. Shikano, and E. Kage-Nakadai, Real-time nanodiamond thermometry probing in vivo thermogenic responses, Sci. Adv. **6**, eaba9636 (2020).

[68] M. Parashar, D. Shishir, A. Bathla, A. Gokhale, S. Bandyopadhyay, and K. Saha, Lock-in detection based dynamic widefield magnetometry using quantum defects in diamond (2021), ArXiv:2107.12232.

[69] M. Turner, Ph.D. thesis, Department of Physics, Harvard University, 2020.